Progress In Electromagnetics Research C, Vol. 112, 21–34, 2021

Simultaneous Measurement of Temperature and Strain Using Multi-Core Fiber with In-Line Cascaded Symmetrical Ellipsoidal Fiber Balls-Based Mach-Zehnder Interferometer Structure

Farhan Mumtaz[1, 2, 3, *], Hongfeng Lin[1], Yutang Dai[1, *], Wenbin Hu[1], Muhammad A. Ashraf[3], Lashari G. Abbas[1, 2], Shu Cheng[1], and Pu Cheng[1]

Abstract—Simultaneous measurement of temperature and strain using multi-core fiber (MCF) with an in-line cascaded symmetrical ellipsoidal fiber balls structure of Mach-Zehnder interferometer (MZI) is presented. The sensor is fabricated by using an ordinary fusion apparatus. The thermo-coupling effect is realized through Germanium (Ge)-doped central and hexagonal distributed outer cores of MCF. A high-quality transmission spectrum is obtained with a fringe visibility of 12–15 dB and higher extinction ratio. The sensor exhibits superior mechanical strength compared with the fragile structures, such as tapered, etched, misaligned and offset fibers. The temperature sensitivity of 137.6 pm/°C and 68.1 pm/°C in the range of 20–90°C, and the strain sensitivity of -0.42 pm/με and -1.19 pm/με in the range of 0–801 με are obtained, when probe "L" is 40 mm and 20 mm, respectively. Simultaneous measurement of temperature and strain can be achieved by solving the coefficient matrix and tracing the wavelength shifts in the interference spectrum. Besides, the sensor has many advantages, such as high sensitivity, easy fabrication, simple structure, being stable and inexpensive, which may find potential applications in the field of optical sensing.

1. INTRODUCTION

Optical sensors are the diversify class implemented in numerous practical applications that are used to detect, quantify, and investigate different physical quantities by light matter interactions. Specifically, while biomedicine, biomedical apparatus biocatalysts, and bionics are studied, these applications need accuracy during quantification and investigation of several physical quantities, i.e., temperature, strain, and refractive index. More precise detection of these physical quantities is quite possible with high resolution devices [1–3]. So far, various sensors by means of electronic [4] and optical [5] devices have been introduced. Due to advantageous features of optical sensors, they have taken precedence over electronic sensors because of high sensitivity, compact size, anticorrosive, high resolution detection, and all of above immunity to electromagnetic interference [6]. In the real world, optical sensors are becoming an ideal choice for industries and scientific societies because of their numerous features and enabling their integration with a wide range of applications.

In optical sensing, MZI composed of pure silica fibers exhibits relatively low sensitivity due to the low thermo-optic coefficient. Whereas, MZI composed of Ge-doped fibers has a high thermo-optic coefficient and displayed high sensitivity. Several traditional MZI sensors based on cascaded, spatial multipath, and linear fiber structures have been reported [7–10], enhancing the characteristics of sensitivity, loss, stability, and reusability. Besides, a few MZI inline-fiber sensors have been reported by

Received 10 February 2021, Accepted 6 April 2021, Scheduled 13 April 2021

* Corresponding authors: Farhan Mumtaz (mfmawan@yahoo.com; mfmawan@whut.edu.cn); Yutang Dai (daiyt6688@whut.edu.cn).
[1] National Engineering Laboratory for Fiber Optic Sensing Technology, Wuhan University of Technology, Luoshi Road 122#, Wuhan 430070, China. [2] School of Information and Communication Engineering, Wuhan University of Technology, Luoshi Road 122#, Wuhan 430070, China. [3] Communications Lab., Department of Electronics, Quaid-i-Azam University, Islamabad 45320, Pakistan.

various methods of fabrication, such as up and down tapering [11, 12] mode-field or core mismatch [13] and femtosecond laser micromachining [14, 15]. Particularly, the equipment of a tapering machine and femtosecond laser is relatively expensive, and its low throughput still limits it to several applications. Besides, a few structures based on photonic crystal fibers (PCF) [5, 16–19] are built up by liquid-infiltration methods. These structures substantially enhance the sensitivity but show disadvantages of fragility, reduced strength, etc. However, the fabrication of these structures involves multiple complexities, such as the complex setting, tool alignment, and accuracy. Zhao et al. [5] have explored twin-core of photonic crystal fiber interferometer for simultaneous measurement of multi-parameters. They achieved maximal sensitivities of 10.89 nm/m^{-1}, 1.24 pm/με, and 73.9 pm/°C for curvature, strain, and temperature, respectively. Zhan et al. [20] have experimentally demonstrated an MZI based on a few-modes multi-core structure. In order to address the cross-sensitivity issue, they used MCF with FAN-IN and FAN-OUT and achieved temperature sensitivity of 105.8 pm/°C and 223.6 pm/°C, and strain sensitivity of 13.96 pm/με and 11.7 pm/με. However, sensitivity of the sensor is relatively high but with the disadvantage of elongated probe. Further, in-line fiber peanut shape structures have been demonstrated by different research groups, as cited in [21–24]. Wu et al. [21, 22] have formed an MZI structure using peanut-shape balls in a single-mode fiber and presented temperature and strain sensitivities of only 46.8 pm/°C and 1.4 pm/με, respectively. Sun et al. [23] have explored an MZI of abrupt taper in PCF and reported temperature sensitivity lower than that of Fiber Bragg Grating (FBG). Yu et al. [24] have solved a wavelength-dependent and phase-dependent feature matrix to measure the refractive index (RI) and temperature response, and presented temperature sensitivity up to 70.9 pm/°C. However, in the research direction of temperature and strain sensing, FBG [25] finds a dominating optical probe, which has good performance of reliability, compatibility, and can be embed in several practical applications without comprising the fiber resistance, but shows the constraints of low sensitivity.

In this paper, a unique design of an MZI sensor based on the MCF with an in-line cascaded symmetrical ellipsoidal fiber balls structure is proposed. The structure can be used to measure temperature and strain simultaneously. Besides, it is simple, easy to fabricate, inexpensive, stable, highly sensitive, and can also address the issues of cross-sensitivity.

The rest of the paper is organized as follows. In Section 2, working principle, simulation, and fabrication are discussed. Interference spectra and experimental results are demonstrated in Section 3.

2. PRINCIPLE AND FABRICATION

2.1. Working Principle

The schematic diagram of the proposed sensor is shown in Figure 1. In order to study the working principle of proposed MZI, the optical path difference of MCF is considered that is caused by the effective refractive index difference between the center and outer core modes. These modes follow the spatial optical path while propagating through the MCF. When these modes interact with each other, as a result, they can produce strong or weak interference which depends upon the strength of modes. In the case of proposed sensor, the interference pattern is mainly formed because of the difference between the spatial optical path of center and outer core modes that propagate along the MCF, longitudinally. Cladding modes support the coupling among center to outer core modes. Thus, the total light intensity

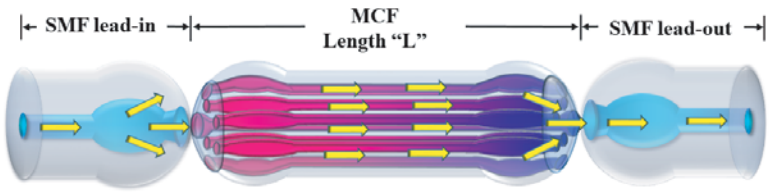

Figure 1. Schematic diagram of the MZI sensor based on MCF with in-line cascaded symmetrical ellipsoidal balls structure.

of sensor at the output can be expressed as [26],

$$I = I_1 + I_2 + 2\sqrt{I_1 I_2}\cos(\Delta\varphi) \tag{1}$$

where I_1 is the light intensity of center core mode, I_2 the intensity of outer cores mode, and $\Delta\varphi$ the phase difference between center and outer cores modes, which can be estimated as,

$$\Delta\varphi = \frac{2\pi\Delta n_{eff} L}{\lambda} \tag{2}$$

where λ is the operating wavelength, Δn_{eff} the effective refractive index difference between the center and outer cores modes, and L the sensing length of the sensor. When the interference dip reaches minimum intensity, the phase difference $\Delta\varphi$ across the cores should satisfy the following condition as,

$$\Delta\varphi = (2m+1)\pi, \quad for\ m = 1, 2, 3, \ldots \tag{3}$$

When the interference spectrum experiences shift because of the change in temperature or strain, resultantly, the m-th order interference dip in the wavelength domain of proposed MZI structure can be traced as,

$$\lambda_m = \frac{2\Delta n_{eff} L}{(2m+1)} \tag{4}$$

Free Spectral Range (FSR) of the interference dips can be determined by the optical path difference of $\Delta n_{eff} L$, which can be approximated as [27],

$$\text{FSR} \approx \frac{\lambda_m^2}{\Delta n_{eff} L} \tag{5}$$

FSR determines the transmission spectrum of the sensor. According to theory, we come to know that when the sensing length L of the sensor increases, the FSR decreases or vice versa.

2.2. Simulation

The transverse energy field distribution inside the ellipsoidal fiber balls is simulated by COMSOL multiphysics ® software. The simulated profile of fibers is obtained at the operating wavelength of 1550 nm, and the simulations parameters of the fibers are listed in Table 1. Figure 2(a) depicts the propagation of fundamental super-mode [28] in the MCF. Figure 2(b) shows the MCF modal profile of cladding mode which is used to contribute the impact of coupling phenomena among center to outer core modes. Likewise, Figure 2(c) depicts the modal profile at SMF Lead-in, and Figure 2(d) illustrates that when light reaches the first SMF ellipsoidal ball the fiber excites cladding mode due to enlargement of fiber waist. However, in the simulation, the fiber balls of ellipsoidal in shape are used with a diameter of 160 µm, which are supposed to be same as actual sensor. These ellipsoidal balls are formed with pre-set arc discharge method of splicing device.

Table 1. Simulation parameters.

Fiber parameters		**Before prefuse discharge**		**After prefuse discharge**	
		SMF	MCF	SMF	MCF
Diameter	Core (µm)	8.9	6.1	11.52	7.8
	Clad (µm)	125	125	160	160
Pitch	Λ (µm)	nil	35	nil	44.8
Refractive index	Core	1.4620	1.4681	1.4620	1.4681
	Clad	1.4570	1.4628	1.4570	1.4628

Further, beam propagation module of the R-soft software is used to investigate the power distribution of mode field with and without in-line ellipsoidal fiber balls in the configuration. Two different probes are used in simulations (i.e., 20 mm & 40 mm). A simulated profile of sensors without

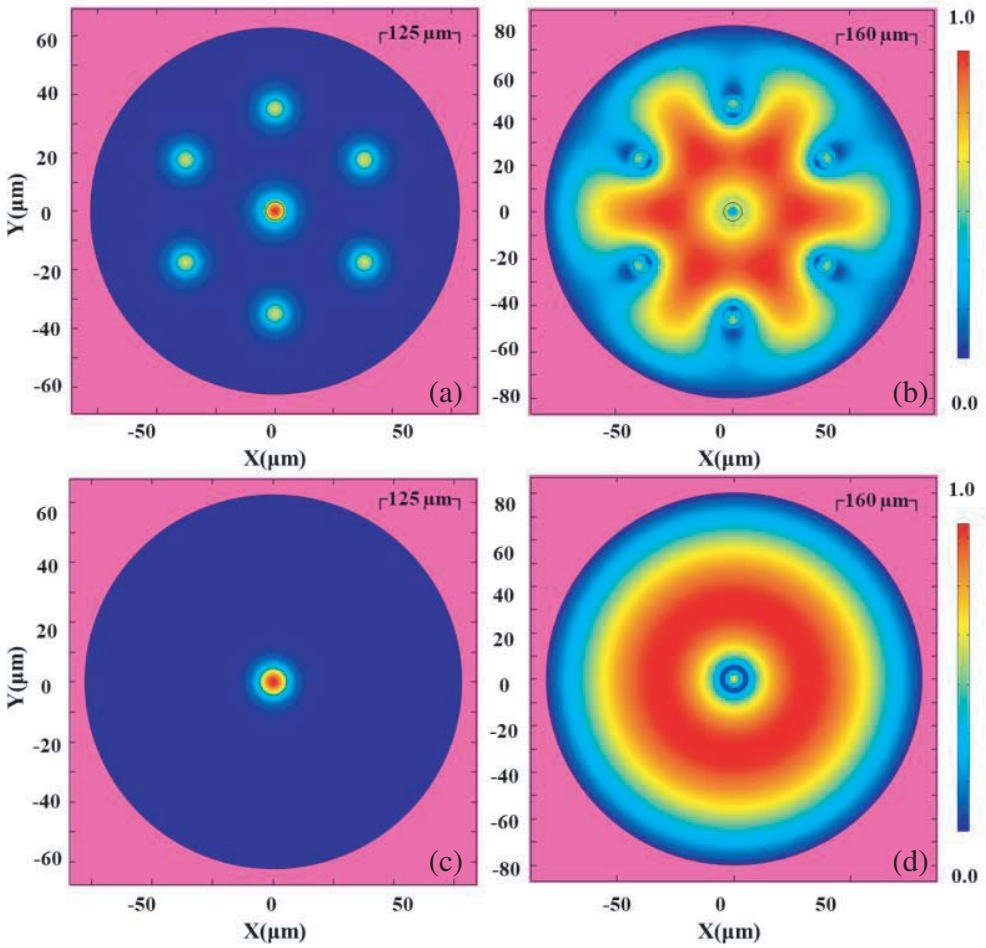

Figure 2. Simulated transverse mode distribution of a normalized electric field, (a) when MCF has original diameter of 125 µm, and (b) when the light reaches at the mid-section of MCF ellipsoidal ball with diameter of 160 µm, then it excites cladding modes, (c) SMF lead-in mode profile with original diameter of 125 µm, and (d) when the light reaches at the mid-section of SMF ellipsoidal ball with diameter of 160 µm and excites cladding mode.

in-line ellipsoidal fiber ball show that when the incident light entered from SMF lead-in to MCF, it is completely confined into the fiber cores, as shown in Figures 3(a) and (c). As expected, a weak interference is seen due to the core mismatch of SMF and MCF, but no significant loss occurs in the transmission. On the other hand, when a sensor with in-line configuration of cascaded ellipsoidal fiber balls is simulated, a large multimode interference is induced, due to greater mismatch at the section∼(F1-F2). The mismatch mode field excites the higher order modes. These higher order modes degenerate in intensity due to different phases across the outer cores while propagating through MCF. Only the fundamental super-mode consisting of center core mode and outer cores mode can propagate through MCF due to the circular symmetry of the cores, as shown in Figure 2(a). Figure 3(b) and Figure 3(d) demonstrate that the light is coupled from center to outer core of MCF at the section∼F2. The light is no more confined into the center core of MCF but also spread into outer cores and cladding region. Finally, when the light reaches the section∼(F2-F3), it recouples back toward SMF lead-out to become a part of stronger interference. It can be inferred that the sensor produces good strong interference, as the multimode and mode coupling are enhanced due to the excitation of cladding mode. Thus, the proposed sensor is a good candidate in promoting better interference spectra in the field of optical sensing.

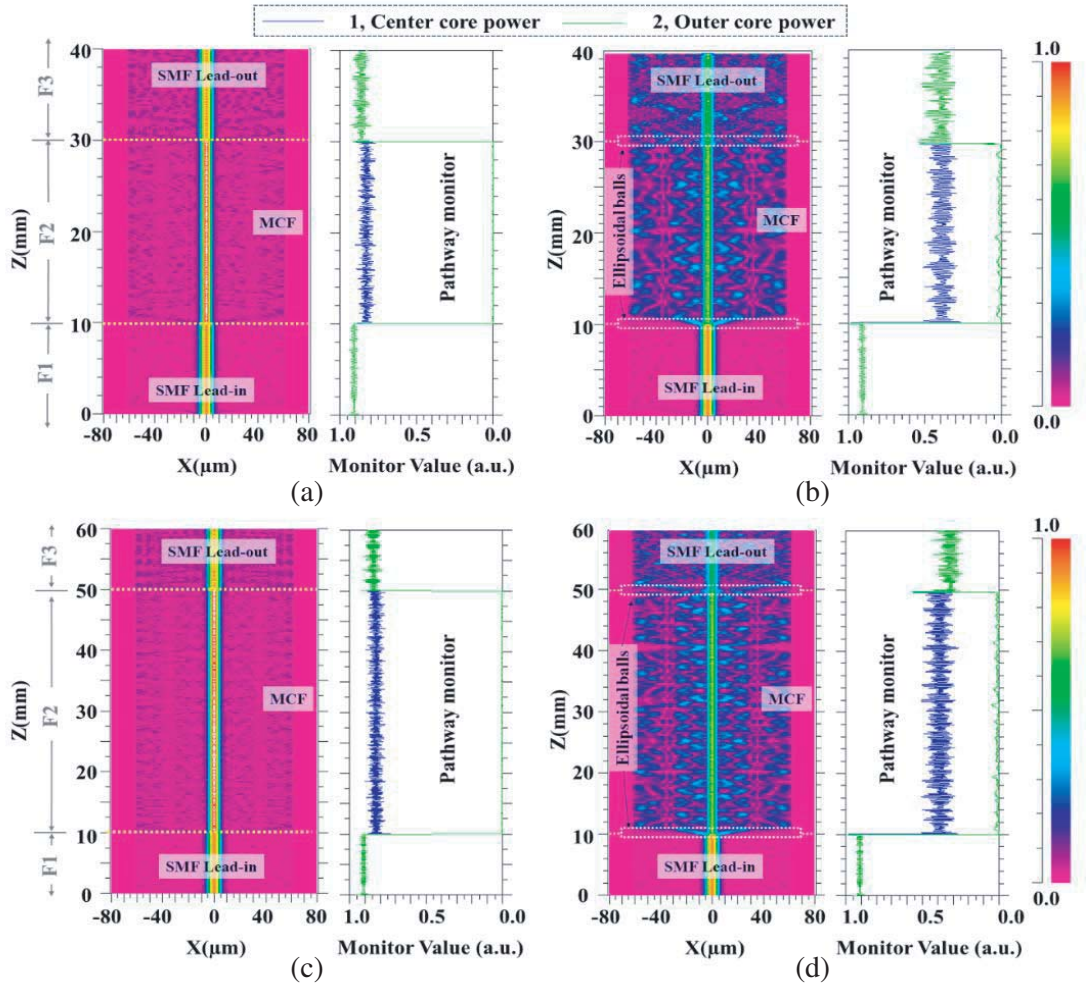

Figure 3. Simulated power distribution of two different MZI structures by a beam propagation tool for $L = 20$ mm (a) without ellipsoidal balls, (b) with ellipsoidal balls; and for $L = 40$ mm (c) without ellipsoidal balls, (d) with ellipsoidal balls sensor.

2.3. Fabrication of Sensor

An MCF (FIBERCORE-SM-7C1500) is used as sensing probe. A commercial single-mode fiber (SMF-28e) is used for Lead-in and Lead-out. The sensor is fabricated using a commercial fusion splicer (Furukawa Fitel S177) through a controlled arc power in the splicer menu. The sensor can be constituted by the following steps. Step-1: an independent fusion is performed at the cleaved end faces of the SMF and MCF. A controlled arc power of +100 bit and a fusion time of 750 ms are used, so that the ends of SMF and MCF would become ellipsoidal fiber balls, as shown in Figures 4(a) & (b), respectively. Step-2: Then these pre-fused end faces of SMF and MCF are spliced together with an arc power of +50 bit and fusion time of 400 ms, so that the section∼(F1–F2) could be formed, as shown in Figure 4(c). Step-3: The MCF is then cleaved at a desired length L, i.e., 20 mm & 40 mm. Similarly, by repeating step-1 and step-2 at the cleaved end faces of MCF and SMF, the rest of the section∼(F2–F3) could be formed to complete the fabrication of the sensor, as shown in Figure 4(d) and Figure 5(a). Also, the transverse facets of SMF and MCF before and after pre-fuse discharging under the microscope can be seen in Figures 5(b)–(e), respectively.

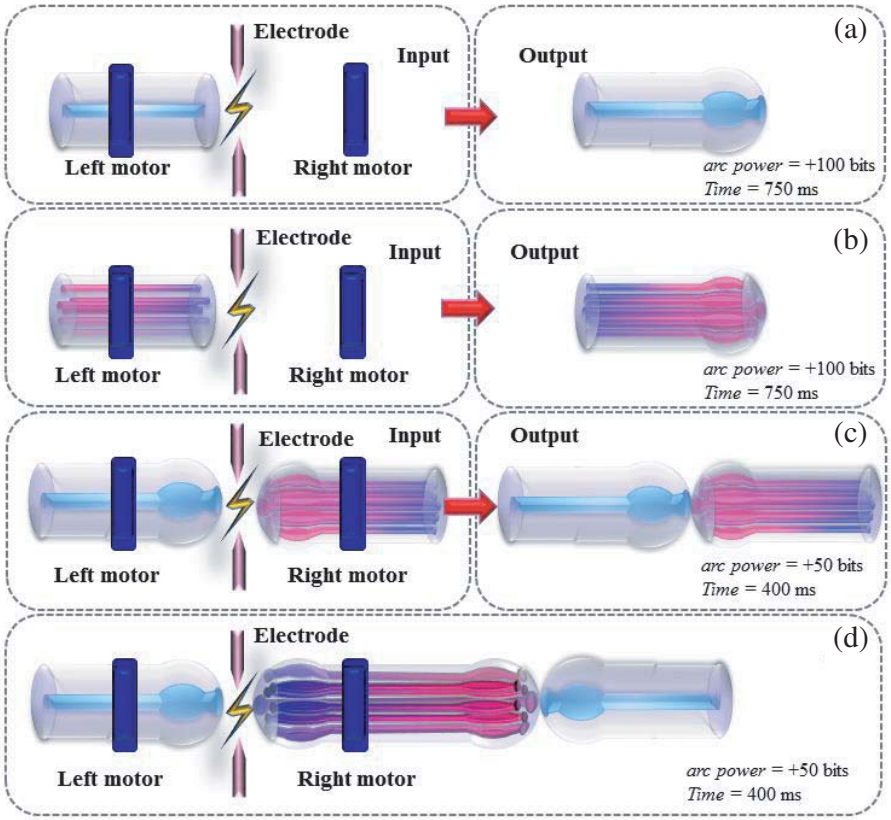

Figure 4. Fabrication steps of a MZI sensor based on MCF with in-line cascaded symmetrical ellipsoidal fiber balls structure, (a) SMF fiber before and after pre-fuse discharge, (b) MCF fiber before and after pre-fuse discharge, (c) a pair of ellipsoidal balls consisting of SMF and MCF is to be spliced by applying arc discharge, and (d) Final splicing segment to assemble the sensor.

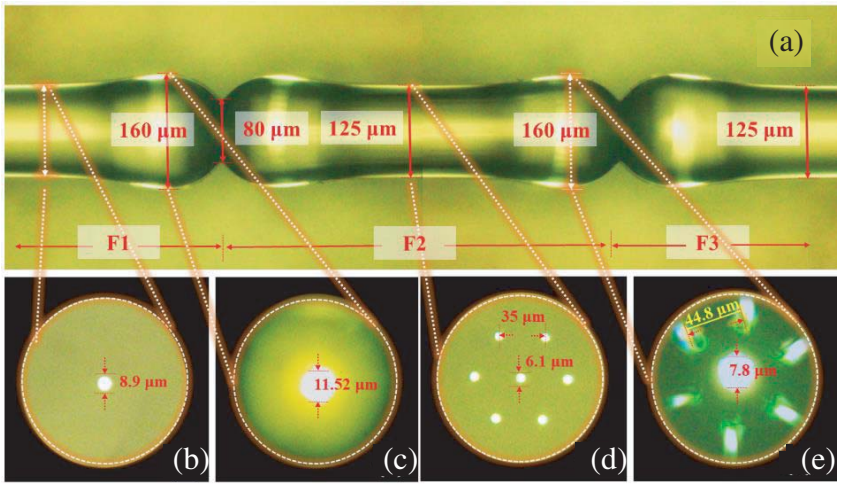

Figure 5. Images under the microscope, (a) Longitudinal cross-section of the proposed MZI sensor, and transverse cross-sections of (b) SMF, (c) SMF with ellipsoidal ball, (d) MCF, and (f) MCF with ellipsoidal ball.

3. EXPERIMENTAL RESULTS AND DISCUSSIONS

3.1. Interference Spectra

The interference spectrum of the proposed sensor is measured with the following setup. A broadband light source (BBS) is used as light sources with a flat band range from 1540 nm to 1600 nm. The spectrum of the sensor is detected using a spectrum analyzer (OSA: YOKOGAWA AQ6370D) with a spectral resolution of 0.02 nm. The interference spectrum consists of two fundamental super-modes. These super-modes are dominant due to the circular symmetry of hexagonal distributed cores in MCF. The traced interference spectrum for probe $L = 20$ mm & 40 mm can be seen in Figure 6(a). Fast Fourier transform is performed on the transmission spectrum of the sensor to obtain a spatial frequency spectrum, as shown in Figure 6(b). Evidently, the spatial frequency spectrum also explains that the interference mainly includes two different modes, dominant center core mode and outer cores mode to form an interference spectrum.

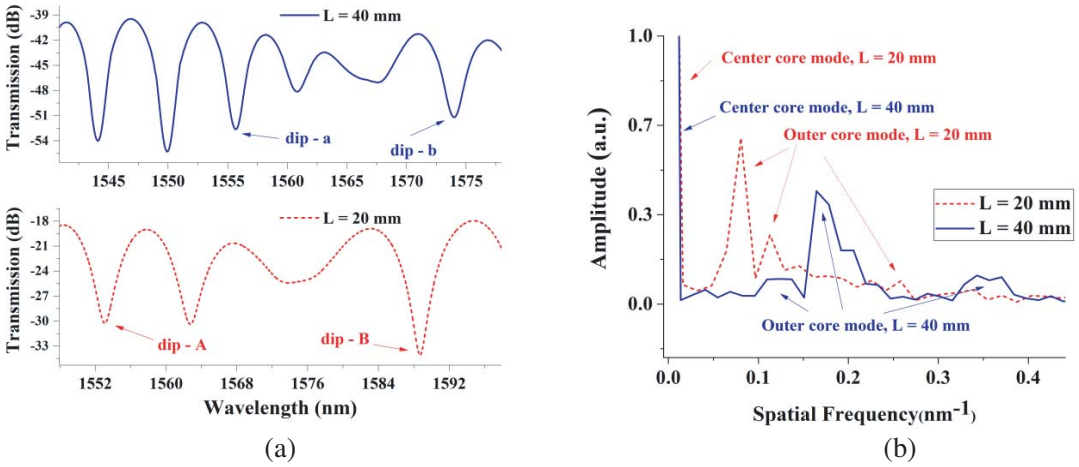

Figure 6. (a) The transmission and (b) the spatial frequency spectra of the sensor.

3.2. Temperature Sensing Response

The change in the effective refractive index of the m-th order interference dip produces a shift with the environment temperature change. The MZI interference is obtained from two distinct splitting light beams. In order to measure temperature response, the resonant interference dip of an MZI principle of interferomer can be estimated as [9],

$$\frac{d\lambda}{dT} = \frac{\lambda}{\Delta n_{eff}} \left(\frac{n_{eff1}}{dT} - \frac{n_{eff2}}{dT} \right) \tag{6}$$

where n_{eff1} and n_{eff2} represent the effective refractive indices of involved super-modes.

The schematic experimental setup of the proposed sensor for temperature measurements is shown in Figure 7. The sensor was placed into a temperature furnace, whose temperature error was approximately 0.01°C. During each temperature shift, the temperature was kept constant for 20 mins. Two different sensors ($L = 20$ mm & 40 mm) were used in the experiment. The experimental results show that when the temperature rose from 20 to 90°C, the interference dips were shifted toward longer wavelength and produced a red-shift. The temperature response of each sensor was measured at two different resonant dips, as shown in Figure 6(a). The temperature sensitivities are obtained as 51.9 pm/°C (dip-A) & 68.1 pm/°C (dip-B) and 137.62 pm/°C (dip-a) & 102.74 pm/°C (dip-b) in the range of 20–90°C, for $L = 20$ mm and 40 mm, as shown in Figures 8(e)–(f), respectively. However, the dips shift response of each sensing length with surrounding temperature change can be seen in Figures 8(a)–(d). All the resonant dips produce a good linearity response of approx. 0.99. Since thermo-optic coefficient of Ge-doped silica core is higher than that of fused silica cladding [29], the wavelength is shifted toward

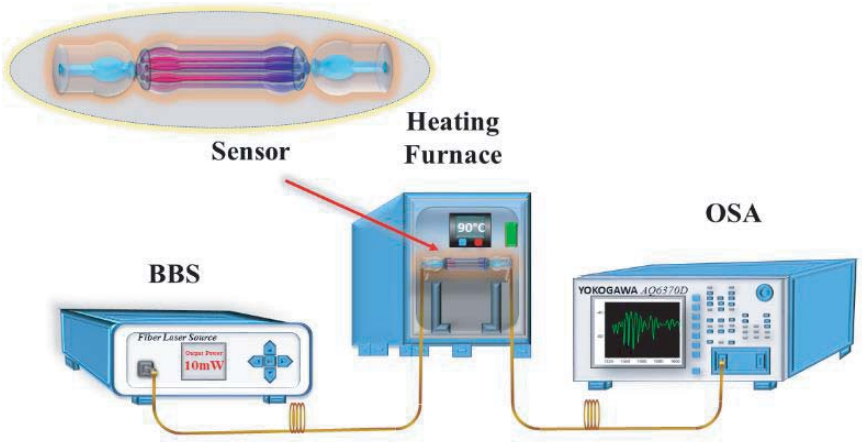

Figure 7. The schematic experimental setup of temperature sensing.

longer wavelength with temperature rose, because of Δn_{eff}, according to Eq. (6). Experimental results demonstrate that the sensor ($L = 40\,\text{mm}$) exhibits optimal sensitivity of 137.62 pm/°C in the range of 20–90°C.

In order to measure the stability response, the sensors were tested at constant temperature for about 60 mins, and dips fluctuations were recorded after every 5 mins. Firstly, the sensors were investigated at 30°C and then 50°C, as shown in Figures 9(a) and (b), respectively. The standard deviation of the wavelength of resonant dips is found in the range of 0.01 nm to 0.021 nm, which indicates that the sensors have good stability.

3.3. Strain Sensing Response

When the axial strain is applied along the sensor, the resonant dips are shifted toward shorter wavelength and produce a blue-shift. From Eq. (4), when the resonant dips of an MZI experience axial strain, the change in wavelength can be calculated as [30],

$$\Delta\lambda_m = \left[1 + \left(\frac{L}{\Delta n_{eff}}\right)\left(\frac{\partial\left(\Delta n_{eff}\right)}{\partial L}\right)\right]\lambda_m\varepsilon \tag{7}$$

Eq. (7) demonstrates that the strain sensitivity is closely related to Δn_{eff}, which is induced by the elongated MCF length L under the axial strain $\partial(\Delta n_{eff})/\partial L$. Meanwhile, when the axial strain ($\mu\varepsilon$) is applied, a slight physical drift will be generated at the splicing joints of ellipsoidal balls. Thereafter, the output light will slightly change with the applied strain.

The schematic experimental setup of the proposed MZI sensor for strain measurements is shown in Figure 10. As the sensor was relocated from a stable glass platform to a movable fiber holder for strain measurement, the transmission spectrum of the sensors was changed in intensity to some extent, but the FSR remains unchanged. The distance between the movable fiber holder was maintained as $\zeta = 30\,\text{cm}$ to measure axial strain. The strain sensitivities are obtained as $-1.19\,\text{pm}/\mu\varepsilon$ (dip-A) and $-0.42\,\text{pm}/\mu\varepsilon$ (dip-B), and $-0.40\,\text{pm}/\mu\varepsilon$ (dip-a) and $-0.42\,\text{pm}/\mu\varepsilon$ (dip-b) in the range of 0–801 $\mu\varepsilon$, for $L = 20\,\text{mm}$ & $40\,\text{mm}$, as shown in Figures 11(e)–(f), respectively. However, the dips shift response of each sensing length with different values of applied strain can be seen in Figures 11(a)–(d). It can be observed that the interference pattern has certain linearity and strong dependency on the sensing length. It can be inferred that when the axial strain is applied, the sensor produces a slight shift toward shorter wavelength. Eq. (7) explains the strain-optic coefficients and the Poisson ratio of the MCF [30, 31] and their dependence on L. So, when the sensing length decreases, the sensitivity to axial strain increases. Thus, the sensor with shorten length L exhibits better axial strain sensitivity, as evidenced by experimental results.

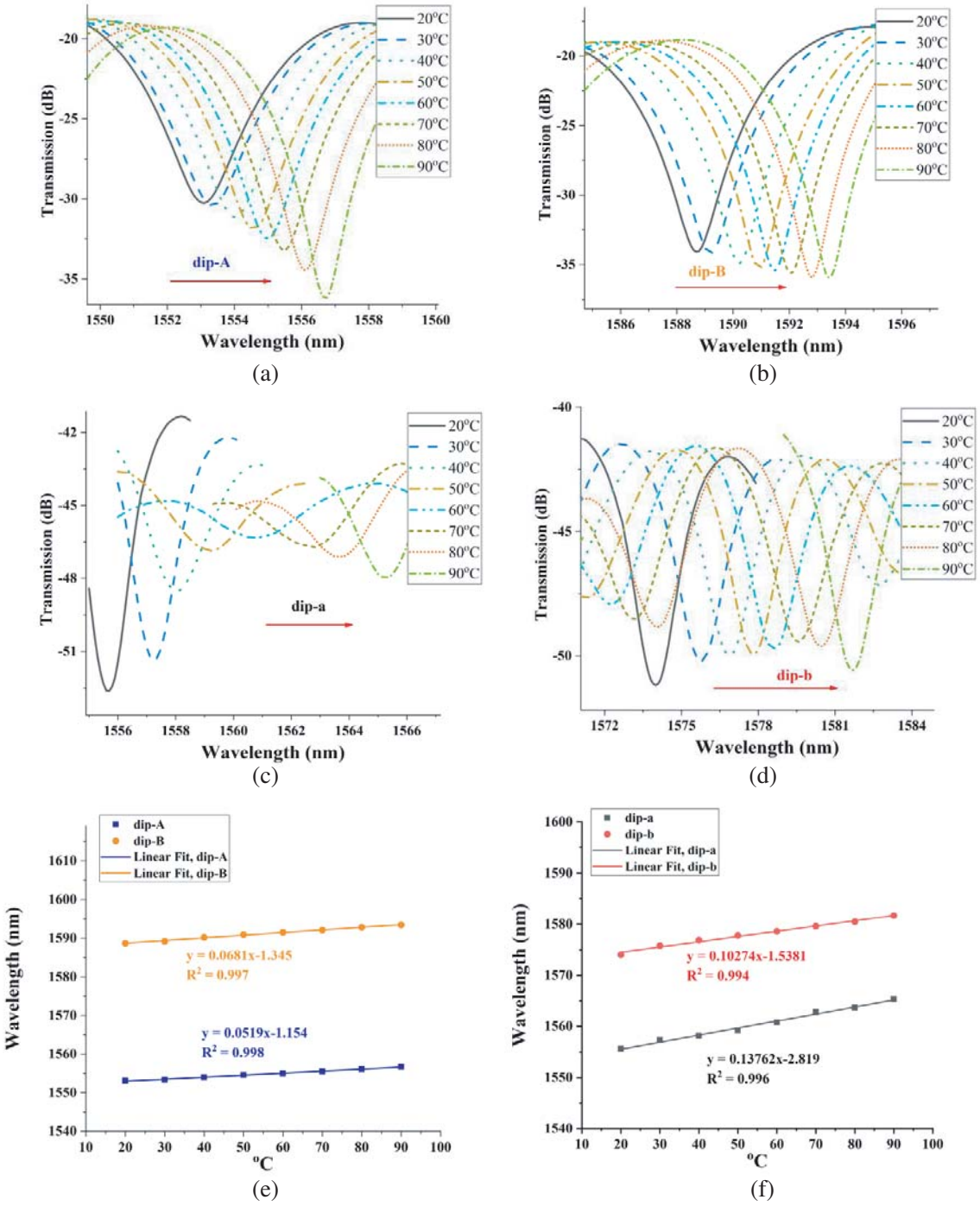

Figure 8. Temperature response and spectral evolution of (a) dip-A and (b) dip-B for sensing $L = 20\,\text{mm}$; spectral evolution of (c) dip-a and (d) dip-b for sensing $L = 40\,\text{mm}$; (e) Linear fit response of dip-A and dip-B for sensing $L = 20\,\text{mm}$; (f) Linear fit response of dip-a and dip-b for sensing $L = 40\,\text{mm}$.

3.4. Simultaneous Measurement of Temperature and Strain by Coefficient Matrix

The transmission spectrum of the sensor is shifted when the temperature and strain are applied to it. The interference dips have different responses from these external physical quantities but shift linearly. The linear superimposition of the resulting wavelength is observed when two parameters are measured

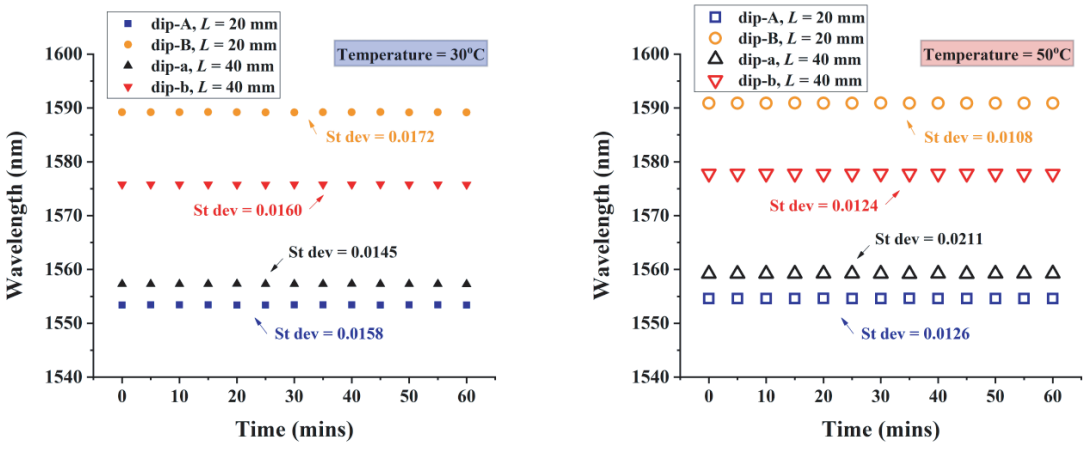

Figure 9. Stability response of the sensor, the resonant dips are recorded at the constant temperature; (a) 30°C, and (b) 50°C.

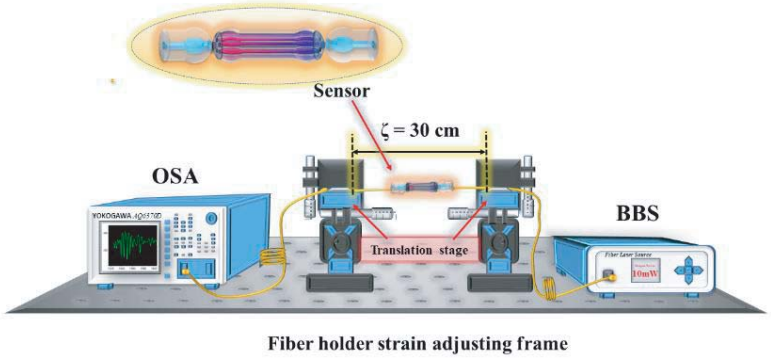

Figure 10. The schematic experimental setup of strain sensing.

simultaneously. So the changes in the wavelength of the interference dips depend on applied temperature and strain, which can be expressed as [5, 32],

$$\Delta\lambda_i = \kappa_{Ti}\Delta T + \kappa_{Si}\Delta S; \quad i = dip\text{-}1 \text{ and } dip\text{-}2 \tag{8}$$

The above equation can be formulated in terms of coefficient matrix as,

$$\begin{bmatrix} \Delta\lambda_{dip\text{-}1} \\ \Delta\lambda_{dip\text{-}2} \end{bmatrix} = \begin{bmatrix} \kappa_{T,dip\text{-}1} & \kappa_{S,dip\text{-}1} \\ \kappa_{T,dip\text{-}2} & \kappa_{S,dip\text{-}2} \end{bmatrix} \begin{bmatrix} \Delta T \\ \Delta S \end{bmatrix} \tag{9}$$

where ΔT and ΔS are the variations of temperature and strain, respectively. $\Delta\lambda$ is the wavelength shift of interference dips, *dip*-1 and *dip*-2. κT and κS are the temperature and strain sensitivities, respectively. By substituting the obtained sensitivities in Eq. (9), the coefficient matrix will have,

$$\begin{bmatrix} \Delta\lambda_{\mathrm{A}} \\ \Delta\lambda_{\mathrm{B}} \end{bmatrix} = \begin{bmatrix} 0.0519 & -0.00119 \\ 0.0681 & -0.000427 \end{bmatrix} \begin{bmatrix} \Delta T \\ \Delta S \end{bmatrix}; \quad for\ L = 20\,\mathrm{mm} \tag{10}$$

$$\begin{bmatrix} \Delta\lambda_{\mathrm{a}} \\ \Delta\lambda_{\mathrm{b}} \end{bmatrix} = \begin{bmatrix} 0.1376 & -0.000401 \\ 0.1027 & -0.000427 \end{bmatrix} \begin{bmatrix} \Delta T \\ \Delta S \end{bmatrix}; \quad for\ L = 40\,\mathrm{mm} \tag{11}$$

By taking the inverse of sensitivity matrix from Eq. (10) and Eq. (11), the coefficient matrix of the

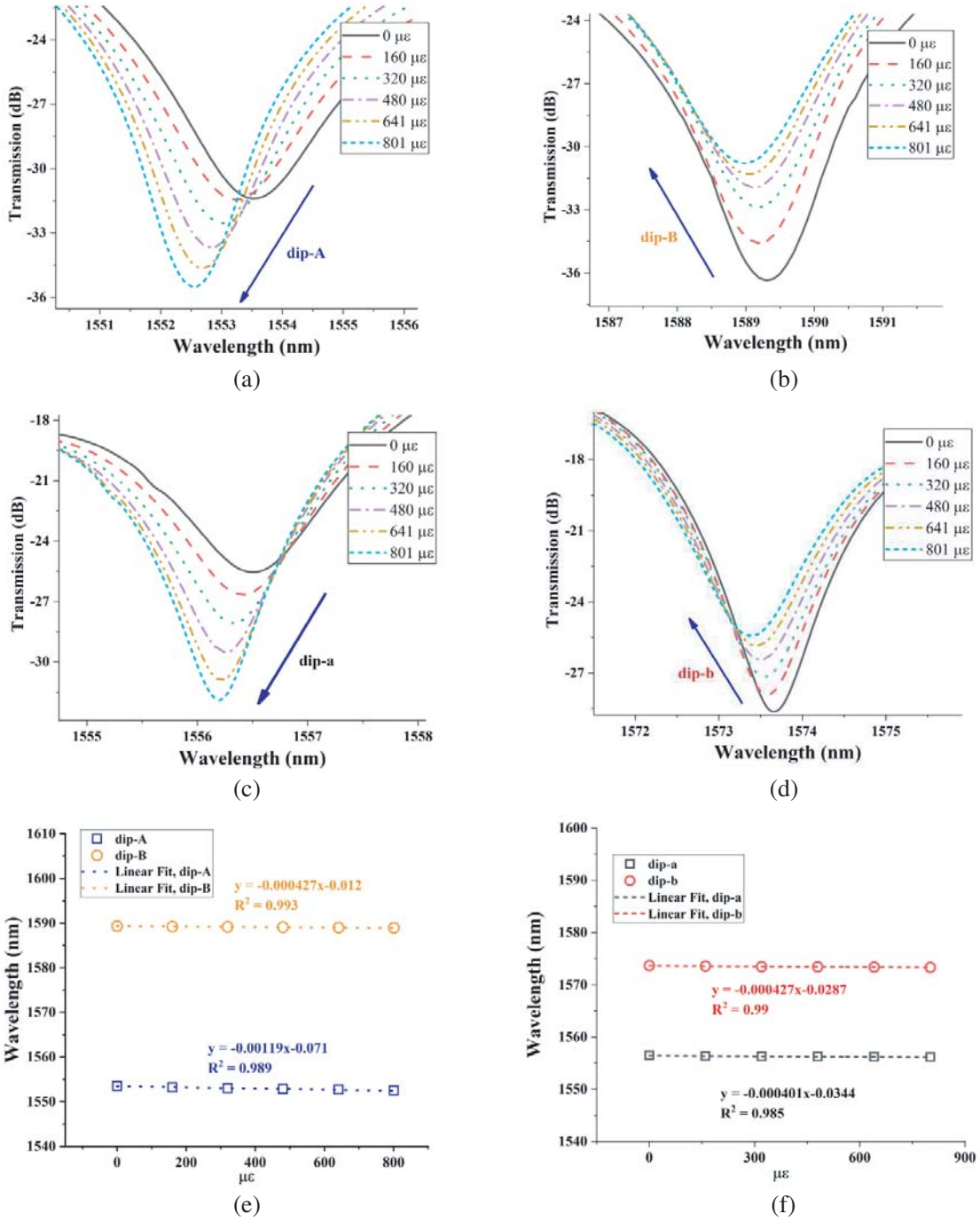

Figure 11. Strain response and spectral evolution of (a) dip-A and (b) dip-B for sensing $L = 20\,\text{mm}$; spectral evolution of (c) dip-a and (d) dip-b for sensing $L = 40\,\text{mm}$; (e) Linear fit response of dip-A and dip-B for sensing $L = 20\,\text{mm}$; (f) Linear fit response of dip-a and dip-b for sensing $L = 40\,\text{mm}$.

proposed sensors for simultaneous measurement of temperature and strain can be calculated as,

$$\begin{bmatrix} \Delta T \\ \Delta S \end{bmatrix} = \begin{bmatrix} -7.25 & 20.21 \\ -1156.6 & 881.48 \end{bmatrix} \begin{bmatrix} \Delta\lambda_{\text{A}} \\ \Delta\lambda_{\text{B}} \end{bmatrix}; \quad \textit{for } L = 20\,\text{mm} \tag{12}$$

$$\begin{bmatrix} \Delta T \\ \Delta S \end{bmatrix} = \begin{bmatrix} 24.29 & -22.81 \\ 5844.35 & -7830.41 \end{bmatrix} \begin{bmatrix} \Delta\lambda_{\text{a}} \\ \Delta\lambda_{\text{b}} \end{bmatrix}; \quad \textit{for } L = 40\,\text{mm} \tag{13}$$

where $\Delta\lambda$, ΔT, and ΔS are expressed in nm, °C, and με, respectively. Thus, ΔT and ΔS can be measured by substituting the change in wavelength $\Delta\lambda$. From Eq. (12) and Eq. (13), the sensitivity matrices state that the proposed sensor is fully capable of simultaneously measuring the changes in temperature and strain by observing the wavelength shifts.

It can be inferred from experimental results that the proposed sensor has higher sensitivity and stability response with good linear correlation than the reported sensors in Table 2. Also the structure can be reproducible, providing similar results.

Table 2. Comparison of the sensor.

Structure type		**Sensitivities**		
		Temperature pm/°C	**Strain pm/με**	**Other**
TCF based on PCF [5]	MZI	73.9	1.24	10.89 nm/m^{-1} (Curvature)
Dual tapering SMF [12]	MZI	65	-	-
Micro-cavity based on SMF [14]	MZI	72.5	−0.98	-
	FPI	0.26	4.24	-
Few mode MCF [20]	MZI	105/223	13.9/11.7	-
Peanut shape, based on SMF [21]	MZI	46.8	1.4	-
Asymmetrical fiber based on PCF [23]	MZI	11.7	-	50.5 nm/m^{-1} (Curvature)
Peanut shape, MZI based on SMF [24]	MZI	70.9	-	−47.3620 nm/RIU (RI)
Fibre Bragg Gratings [25]	FBG	10	0.65	-
This paper	MZI	137.6/68.1	−0.42/−1.19	-

4. CONCLUSION

An MZI sensor based on MCF with an in-line cascaded symmetrical ellipsoidal fiber balls structure is presented to simultaneously measure temperature and strain. A simple approach of a control arc power of splicing device is utilized to fabricate the sensor. The proposed sensor of length $L = 20$ mm & 40 mm exhibits maximal temperature sensitivity of 68.1 pm/°C and 137.6 pm/°C, and strain sensitivity of −1.19 pm/με and −0.42 pm/με with a good linear correlation, respectively. In addition, the sensor shows greater dependency on the sensing length, as the elongated length exhibits better temperature sensitivity than the shortened one, whereas the shortened length presents better strain sensitivity than the elongated one. The sensor is fully capable of simultaneously measuring temperature and strain through the sensitivity coefficient matrix. Easy fabrication, high sensitivity, and high stability can promote the proposed sensor in different potential applications of biomedicine, biomedical apparatus, biocatalysts and bionics.

ACKNOWLEDGMENT

This work was supported in part by the Major Technique Innovation Program of Hubei Province of China under Grant 2018AAA016, in part by the National Key Research and Development Program of China under Grant 2017YFB0405501, and in part by the National Natural Science Foundation of China under Grant 51975442.

REFERENCES

1. Li, S., A. Liu, Z. Yang, L. Zhao, J. Wang, F. Liu, R. You, J. He, C. Wang, X. Yan, and P. Sun, "Design and preparation of the WO3 hollow spheres@ PANI conducting films for room temperature flexible NH3 sensing device," *Sensors and Actuators B: Chemical*, Vol. 289, 252–259, 2019.
2. Dusablon, L., V. Fortin, T. Boilard, M. Bernier, P. Galarneau, F. Babin, and R. Vallée, "High resolution temperature sensor based on frequency beating between twin DFB fiber lasers," *Optics Express*, Vol. 28, No. 18, 26067–26075, 2020.
3. Paixão, T., F. Araujo, and P. Antunes, "High-resolution strain and temperature Fabry-Pérot interferometer sensor based on Vernier effect and produced by a femtosecond laser," *Seventh European Workshop on Optical Fibre Sensors*, Vol. 11199, 111992U, August 2019.
4. Chen, Y., B. Lu, Y. Chen, and X. Feng, "Ultra-thin and ultra-flexible temperature/strain sensor with CNT nanostrips," *2016 IEEE International Conference on Electron Devices and Solid-State Circuits (EDSSC)*, 70–73, August 2016.
5. Zhao, T., S. Lou, X. Wang, W. Zhang, and Y. Wang, "Simultaneous measurement of curvature, strain and temperature using a twin-core photonic crystal fiber-based sensor," *Sensors*, Vol. 18, No. 7, 2145, 2018.
6. Mumtaz, F., Y. Dai, and M. A. Ashraf, "Inter-cross de-modulated refractive index and temperature sensor by an etched Multi-core fiber of a MZI structure," *Journal of Lightwave Technology*, Vol. 38, No. 24, 6948–6953, December 15, 2020, doi:10.1109/JLT.2020.3014857.
7. Zhao, Z., M. Tang, S. Fu, S. Liu, H. Wei, Y. Cheng, W. Tong, P. P. Shum, and D. Liu, "All-solid multi-core fiber-based multipath Mach-Zehnder interferometer for temperature sensing," *Applied Physics B*, Vol. 112, No. 4, 491–497, 2013.
8. Lu, Y., C. Shen, C. Zhong, D. Chen, X. Dong, and J. Cai, "Refractive index and temperature sensor based on double-pass M-Z interferometer with an FBG," *IEEE Photonics Technology Letters*, Vol. 26, No. 11, 1124–1127, 2014.
9. Mumtaz, F., P. Cheng, C. Li, S. Cheng, C. Du, M. Yang, Y. Dai, and W. Hu, "A design of taper-like etched multicore fiber refractive index-insensitive a temperature highly sensitive Mach-Zehnder interferometer," *IEEE Sensors Journal*, Vol. 20, No. 13, 7074–7081, July 2020.
10. Kaur, G. and R. S. Kaler, "Nanohybrid optical sensor for simultaneous measurements of strain, temperature, and vibration for civil application," *Micro & Nano Letters*, Vol. 13, No. 1, 1–3, 2018.
11. Tan, J., G. Feng, J. Liang, and S. Zhang, "Optical fiber temperature sensor based on dumbbell-shaped Mach-Zehnder interferometer," *Optical Engineering*, Vol. 57, No. 1, 017112, 2018.
12. Wang, Q., H. Meng, X. Fan, M. Zhou, F. Liu, C. Liu, Z. Wei, F. Wang, and C. Tan, "Optical fiber temperature sensor based on a Mach-Zehnder interferometer with single-mode-thin-core-single-mode fiber structure," *Review of Scientific Instruments*, Vol. 91, No. 1, 015006, 2020.
13. Huang, B., S. Xiong, Z. Chen, S. Zhu, H. Zhang, X. Huang, Y. Feng, S. Gao, S. Chen, W. Liu, and Z. Li, "In-fiber Mach-Zehnder interferometer exploiting a micro-cavity for strain and temperature simultaneous measurement," *IEEE Sensors Journal*, Vol. 19, No. 14, 5632–5638, July 15, 2019.
14. Li, W. W. and D. N. Wang, "Femtosecond laser inscribed straight waveguide in no-core fiber for in-line Mach-Zehnder interferometer construction," *Optics Letters*, Vol. 43, No. 14, 3405–3408, 2018.
15. Yang, J., S. Wang, X. Chen, X. Zou, Y. Liu, R. Lin, Y. Wang, and Y. Chenl, "Optical fiber Mach-Zehnder interferometric strain sensor basedon concatenating two micro cavities fabricated by a femtosecond laser," *2019 IEEE 10th International Conference on Mechanical and Aerospace Engineering (ICMAE)*, 533–538, Brussels, Belgium, 2019.
16. Liang, H., W. Zhang, H. Wang, P. Geng, S. Zhang, S. Gao, C. Yang, and J. Li, "Fiber in-line Mach-Zehnder interferometer based on near-elliptical core photonic crystal fiber for temperature and strain sensing," *Optics Letters*, Vol. 38, No. 20, 4019–4022, 2013.
17. Zhao, Y., X. Li, L. Cai, and Y. Zhang, "Measurement of RI and temperature using composite interferometer with hollow-core fiber and photonic crystal fiber," *IEEE Transactions on Instrumentation and Measurement*, Vol. 65, No. 11, 2631–2636, November 2016.

18. Han, B., Y. N. Zhang, E. Siyu, X. Wang, D. Yang, T. Wang, K. Lu, and F. Wang, "Simultaneous measurement of temperature and strain based on dual SPR effect in PCF," *Optics & Laser Technology*, Vol. 113, 46–51, 2019.
19. Wang, G., Y. Lu, X. Yang, L. Duan, and J. Yao, "Square-lattice alcohol-filled photonic crystal fiber temperature sensor based on a Sagnac interferometer," *Applied Optics*, Vol. 58, No. 8, 2132–2136, 2019.
20. Zhan, X., Y. Liu, M. Tang, L. Ma, R. Wang, L. Duan, L. Gan, C. Yang, W. Tong, S. Fu, and D. Liu, "Few-mode multicore fiber enabled integrated Mach-Zehnder interferometers for temperature and strain discrimination," *Optics Express*, Vol. 26, No. 12, 15332–15342, 2018.
21. Wu, D., T. Zhu, K. S. Chiang, and M. Deng, "All single-mode fiber Mach-Zehnder interferometer based on two peanut-shape structures," *Journal of Lightwave Technology*, Vol. 30, No. 5, 805–810, 2012.
22. Wu, D., T. Zhu, D. W. Duan, K. S. Chiang, and M. Deng, "In-line single-mode fiber interferometers based on peanut-shape fiber structure," *Proc. SPIE 8421, OFS2012 22nd International Conference on Optical Fiber Sensors*, 84217N, November 7, 2012.
23. Sun, B., Y. Huang, S. Liu, C. Wang, J. He, C. Liao, G. Yin, J. Zhao, Y. Liu, J. Tang, and J. Zhou, "Asymmetrical in-fiber Mach-Zehnder interferometer for curvature measurement," *Optics Express*, Vol. 23, No. 11, 14596–14602, 2015.
24. Yu, F., P. Xue, X. Zhao, and J. Zheng, "Simultaneous measurement of refractive index and temperature based on a peanut-shape structure in-line fiber Mach-Zehnder interferometer," *IEEE Sensors Journal*, Vol. 19, No. 3, 950–955, 2018.
25. Rao, Y. J., "In-fibre Bragg grating sensors," *Meas. Sci. Technol.*, Vol. 8, 355–375, April 1997.
26. Wang, X., D. Chen, H. Li, G. Feng, and J. Yang, "In-line Mach-Zehnder interferometric sensor based on a seven-core optical fiber," *IEEE Sensors Journal*, Vol. 17, No. 1, 100–104, 2016.
27. Li, L., L. Xia, Z. Xie, and D. Liu, "All-fiber Mach-Zehnder interferometers for sensing applications," *Optics Express*, Vol. 20, No. 10, 11109–11120, 2012.
28. Xia, C., M. A. Eftekhar, R. A. Correa, J. E. Antonio-Lopez, A. Schülzgen, D. Christodoulides, and G. Li, "Supermodes in coupled multi-core waveguide structures," *IEEE Journal of Selected Topics in Quantum Electronics*, Vol. 22, No. 2, 196–207, Art No. 4401212, March–April 2016.
29. Lu, P., L. Men, K. Sooley, and Q. Chen, "Tapered fiber Mach-Zehnder interferometer for simultaneous measurement of refractive index and temperature," *Applied Physics Letters*, Vol. 94, No. 13, 131110, 2009.
30. Villatoro, J., O. Arrizabalaga, G. Durana, et al., "Accurate strain sensing based on super-mode interference in strongly coupled multi-core optical fibres," *Sci. Rep.*, 7, article No. 4451, June 30, 2017.
31. Her, S.-C. and C.-Y. Tsai, "Strain measurement of fiber optic sensor surface bonding on host material," *Transactions of Nonferrous Metals Society of China*, Vol. 19, s143–s149, 2009.
32. Frazão, O., S. O. Silva, J. M. Baptista, J. L. Santos, G. Statkiewicz-Barabach, W. Urbanczyk, and J. Wojcik, "Simultaneous measurement of multiparameters using a Sagnac interferometer with polarization maintaining side-hole fiber," *Applied Optics*, Vol. 47, No. 27, 4841–4848, 2008.